



Final Report

Fabrication and Characterization of Advanced Borosilicate Glasses with Enhanced Mechanical Performance

Lukas Ladinger

Supervisor MUL: Prof. Dr. Raul Bermejo

Supervisor PSU: Prof. Dr. John C. Mauro



Department of Materials
Science and Engineering

Abstract

The designing of new glasses has proven to be a very challenging task due to the various complications and impacts every element in use has for the resulting glass. During this study the impact of a network modifier (NWM) in the form of barium in an aluminoborosilicate (ABS) glass has been investigated. To better understand how the ratio of $[NWM]/[Al_2O_3]$ influences physical and mechanical properties, four different Ba-ABS glass compositions were designed. While the content of barium for every composition differs, the $[SiO_2]/[B_2O_3]$ ratio as well as the portion of $[Al_2O_3]$ stayed constant throughout the series. It has been found that hardness, density and various moduli (Young's, shear and bulk) rise with increasing barium content, properties like crack resistance and indentation fracture resistance decrease. The most probable explanation for this behaviour is the transformation of three coordinated, trigonal (B^{III}) to four coordinated, tetrahedral boron (B^{IV}) via local charge stabilization. The results of this study will deepen the understanding on how the portion of NWM influences the physical and mechanical properties of aluminoborosilicate glasses and therefore help to further tailor ABS glasses for specific applications.

Einleitung

Die Entwicklung neuer Gläser hat sich aufgrund der verschiedenen Komplikationen und Einflüsse, die jedes verwendete Element auf das resultierende Glas hat, als eine sehr anspruchsvolle Aufgabe erwiesen. In dieser Studie wurde der Einfluss eines Netzwerkmodifikators (NWM) in Form von Barium in einem Aluminiumborosilikatglas (ABS) untersucht. Um besser zu verstehen, wie das Verhältnis $[NWM]/[Al_2O_3]$ die physikalischen und mechanischen Eigenschaften beeinflusst, wurden vier verschiedene Ba-ABS-Glaszusammensetzungen entwickelt und hergestellt. Während der Bariumgehalt für jede Zusammensetzung unterschiedlich ist, blieben das Verhältnis zwischen $[SiO_2]/[B_2O_3]$ sowie der Anteil von $[Al_2O_3]$ über die gesamte Serie hinweg konstant. Es wurde festgestellt, dass Härte, Dichte und verschiedene Moduli (Young's, Schub- und Kompressionsmodul) mit zunehmenden Bariumanteilen ansteigen, während Eigenschaften wie Rissfestigkeit und Eindringbruchfestigkeit abnehmen. Die wahrscheinlichste Erklärung für dieses Verhalten ist die Transformation von dreifach koordiniertem, trigonalen (B^{III}) zu vierfach koordiniertem, tetraedrischem Bor (B^{IV}) durch lokale Ladungsstabilisierung. Die Ergebnisse dieser Studie werden das Verständnis dafür vertiefen, wie der Anteil an NWM die physikalischen und mechanischen Eigenschaften von Aluminiumborosilikatgläsern beeinflusst, und somit helfen, ABS-Gläser für spezifische Anwendungen weiter zu optimieren.

Table of content

1	Introduction.....	4
2	Experimental work	6
2.1	Starting materials	6
2.2	Material batching	6
2.3	Sample fabrication, preparation and characterization	7
2.4	Thermal characterization	8
2.5	Hardness.....	8
2.6	Echography and density	10
2.7	Probability of crack Initiation and crack resistance.....	12
3	Results and discussion.....	14
3.1	Compositions.....	14
3.2	Moduli and density.....	15
3.3	Molar volume and glass transition temperature	19
3.4	Microhardness and indentation fracture resistance K_{IFR}	21
3.4.1	Microhardness results	21
3.4.2	Indentation fracture resistance (K_{IFR})	24
3.5	Crack resistance.....	26
4	Conclusion	29
5	Reference	30

1 Introduction

Glasses are a material group which has been known to men for a long amount of time. While some historians suggest that glasses were first discovered and used between 3000 and 2000 BC, some argue that the origin of glass might have been as early as 8000 BC. [1] Since then, glasses have come a long way and have cemented their role and importance in society. In honour of this, the UN General Council declared 2022 to be the United Nations International Year of Glass. [2]

But what exactly are glasses? Most people would probably answer this question by claiming that glass is a transparent and solid material which shatters in pieces when broken. Since this simple definition is very restrictive and from a scientific point of view even false, Arun K. Varshneya and John C. Mauro attempted in their book "Fundamental of Inorganic Glasses", [3] to make a more suitable definition for what glasses are. In order to do that, they first came up with a few properties glasses exhibit, which they had to cover with their definition:

- Appearance is solid-like
- Imprecise melting-point
- Cleave in non-preferred direction
- Essentially isotropic
- Atomic arrangements must display long-range disorder (liquid-like)

One of their earlier attempts to define glasses reads: "Glass is a solid having a noncrystalline structure which continuously converts to a liquid on heating". [4] This definition, -however, left some room for speculation because it would mean that wax would also count as a glass. After years of research, it was discovered that a glass is neither a true solid nor a true liquid but rather has its own unique state, combining features of liquids and solids. So, the definition was updated and now reads: "Glass is a nonequilibrium, noncrystalline state of matter that appears solid on a short time scale but continuously relaxes towards the liquid state". [3] The term "short time scale" in this definition refers to a time period observable by human time scale. For the purpose of this paper when talking about glasses it is referred to this definition by Arun K. Varshneya and John C. Mauro.

Strong bonds in combination with high chemical stability are just a few characteristics of advanced glasses. Due to these properties, it is no surprise that these materials are well-suited for applications where high temperature stability and mechanical resistance are demanded. [3] One of the most prominent examples utilizing those extraordinary features is Gorilla® Glass. [5] With the development of advanced glasses they have made themselves irreplaceable in other fields such as communication, optics and electronic devices.

Most glass precursors can be divided into two groups. The glass network formers (NWFs), are typically the dominant components and form the backbone for every glass. Commonly used NWFs are for example, SiO_2 , B_2O_3 , or V_2O_5 . Glass network modifiers (NWMs) are used to enhance the properties of the resulting glass by changing the bonding characteristics of the glass structure. Typical modifiers for oxide glasses are Li_2O , MgO , or BaO . For completeness it has to be mentioned that there is a third group called network intermediates, which can act as NWFs as well as NWMs. For example iron (II) behaves more like a NWM while iron (III) acts like a NWF. Since there is still a lot of speculation about those elements and their characteristics, they won't be mentioned any further in this paper. [3]

When designing a new glass composition many things need to be considered. Not only modifying the chemical composition of the glass will lead to alterations, processing as well as manufacturing has a big influence on the final product. Changing the chemical composition of a glass will not only change its final glass attributes but might also change the properties of the glass-forming liquid. [6] Another aspect when designing new glass compositions is that almost every element of the periodic table can be used for glass formation, resulting in an indefinite number of design possibilities. [7] Another complication to the topic of designing glasses comes from the fact that the properties are dependent on the complete thermal and pressure history. [8] Considering all those aspects, the way of developing new glasses is through already existing glasses and altering their compositions in trial and error experiments.

With that in mind, two papers are especially important for this study. One of the papers was written by A. Fry et al. with the title "Field strength effect on structure, hardness and crack resistance in modifier aluminoborosilicate glasses". In her work she examines the effect of different alkali and alkaline earth elements NWMs, on the mechanical properties of ABS glasses. [9] The second paper which gave the idea for this work "Accelerating the Design of Functional Glasses through Modelling" was written by John C. Mauro et al. It discusses the difficulties when designing new glasses and how through a combination of different models, it is possible to design and optimize glass compositions for industrial purposes. [6]

The purpose of the present investigation is to look into the correlation between composition, to be more specific on the portion of a single network modifier, and the mechanical performance of an ABS glass. The idea is that with different amounts of network modifier, the inner structure of the glass will change and thus vary the mechanical properties and enhance the performance of the glass.

Boric oxide (B_2O_3) has proven to be a very reliable network forming constituent (NWF) when designing damage resistance glasses. Low thermal expansion coefficient ($\sim(3 - 6) \times 10^{-6}K^{-1}$), high chemical resistance as well as a favourable impact on optical and mechanical properties are just a few of the reasons, why it has itself established as a premier element in glass design. [3] [6] [10] The most interesting property for the purpose of this work however has to do with the structural appearance of the boron itself. In its basic configuration, B_2O_3 appears in form of boroxol ring structural units consisting of corner sharing BO_3 triangles (B^{III}). [11] [12] When modifier is added to boron containing molecules, it alters in two different ways: [6] [11]

- Creation of nonbridging oxygen (NBO)
- Transformation from trigonal boron (B^{III}) to tetrahedral boron (B^{IV})

Due to their individual characteristics, regarding molar volume and rigidity, these modifications have completely different impacts on the structure of the resulting glass and thus its properties. Trigonal boron has a more open structure and is able to densify a bit more compared to its tetrahedral counterpart due to the transformation of B^{III} to B^{IV} under stress. It is desirable for high damage resistance applications to have a higher portion of B^{III} . On the other hand B^{IV} creates a much denser and stiffer structure, which is also favourable for other applications.

In order to see how the portion of NWM added to the ABS changes the outcome of B^{III} and B^{IV} respectively, one network modifier was picked and several compositions varying in the ratio of NWF to NWM were created and analysed.

For this work barium was used as the NWM added to the ABS glasses. There are a few reasons why this alkaline earth metal was chosen. It is one of the NWMs used in previous work by A. Fry et al. and it is commercially used in glass making since it increases the refractive index and the luster of the resulting glass. [9] [13] Barium as NWM was also chosen based on personal experiences with it during other in-process work.

2 Experimental work

2.1 Starting materials

All samples and tiles for this work were fabricated out of the same five starting chemicals. The purity, manufacturer as well as the product number can be seen in Table 1.

Table 1 Overview starting chemicals

Chemical	Manufacturer	Purity %	Lot#
SiO_2	Alfa Aesar	99,5	N06F034
H_3BO_3	Thermo Scientific	≥ 99	A0436197
Al_2O_3	Acros Organic	99,7	A0406764
BaCO_3	Aldrich Chemical Company	≥ 99	09923MX
SnO_2	Acros Organic	99	A0353554

2.2 Material batching

The different compositions used were calculated in mole percent. While the portion of network modifier changed with different compositions (e.g. 14% NWM or 16% NWM), the portion of Al_2O_3 stayed at a constant 10%. Furthermore, the ratio between B_2O_3 and SiO_2 was held at a constant 0.63. Table 2 shows in detail the names of the compositions as well as the planned mole percent of the different components.

Table 2 Batch Compositions and their desired mole percent

Name	SiO_2 [%]	B_2O_3 [%]	Al_2O_3 [%]	BaO[%]	SnO_2 [%]
Ba10	48,98	30,77	10,00	10,00	0,25
Ba14	46,52	29,23	10,00	14,00	0,25
Ba16	45,29	28,46	10,00	16,00	0,25
Ba22	41,61	26,14	10,00	22,00	0,25

To weigh in the chemicals, according to a batch sheet, their desired mole percent were converted to a mass and combined in a Nalgene bottle. An example for the necessary masses for a 50g batch is

given in Table 3. To properly mix the components together, the Nalgene bottles were shaken up to ten, but at least five minutes by hand. This process made the batch easier to transfer into the crucible, and also resulted in better mixing of the raw materials. Afterwards, the bottles were sealed with a Parafilm to minimize water adsorption.

Table 3 Example Masses for a Composition

Name	SiO ₂ [g]	H ₃ BO ₃ [g]	Al ₂ O ₃ [g]	BaCO ₃ [g]	SnO ₂ [g]	Total [g]
Ba14	13,66	17,67	4,98	13,50	0,18	50

2.3 Sample fabrication, preparation and characterization

Mixed batch powders were melted using an electric furnace (Deltech Inc., Denver, CO, USA). The powders were poured into a 90%Pt/10%Rh crucible and heated up to a maximum temperature of 1680°C. The materials dwelled at the temperature for 2h before being quenched on a steel plate. To ensure homogeneity, the fabricated glass was crushed and remelted for another hour at 1680°C. The melt was poured into a mold on a steel plate with rated flatness to achieve the desired geometry.

A portion of the resultant glass was used to make a powder by grinding for 45 seconds at 750 rpm with the help of a ceramic pulveriser. The fabricated powders were used later for thermal and compositional analyses.

Before further steps could be done, it was necessary to anneal the bars at a temperature roughly $0.92 \cdot T_g$ for five hours. This was accomplished using an electric furnace (CM Furnaces, Inc, Bloomfield, NJ, USA). The reason behind this step was to remove the inner thermal stresses, which were induced during the quenching of the glass bars. The effects of the annealing process can be seen in Figure 1. In the left picture of Figure 1 the unannealed bar can be seen under a polarizer. The different colours showcase by the sample, hint there are inner stresses within the bar. On the right side, the bar can again be seen under a polarizer. This time no colours can be observed meaning, the inner stresses are gone and the annealing process was a success.



Figure 1 Ba16#1 as-quenched, unannealed (left) and annealed (right)

Finally, the annealed bars were cut into small squares with an approximate cross-section of 1,5x1,5cm using a Techcut4 slow speed saw (Allied High Tech Products Inc., Compton, CA, USA). The last step of preparation consisted of cleaning the samples. This was done by putting the samples in an Acetone filled container which was then placed in an ultrasonic bath.

The glassy state of the resulting products was confirmed via X-ray diffraction analysis (XRD). Copper was the element used to produce the radiation with a wavelength of 1.54059Å.

To determine the actual chemical composition of the produced glasses, a small amount of each composition was analysed via inductively coupled plasma atomic emission spectroscopy (ICP). The samples were dissolved by lithium metaborate fusion and run on a Thermo iCAP 7400 ICP (Thermo Fisher Scientific, Waltham, MA, USA).

2.4 Thermal characterization

The glass transition temperatures (T_g) for the individual compositions were obtained via differential scanning calorimetry (DSC). The machine used for this task was a TA Instruments SDT Discovery 650 (TA Instruments, New Castle, DE) and the data was evaluated utilizing the TRIOS software. To conduct the experiment, a small amount of powder was put into an alumina pan with a lid. Afterwards, the pan was placed into the DSC and heated up to a maximum temperature before cooling down again. This procedure was done for every composition. Samples were scanned using only one heat up sequence since it appeared that phase separation took place during the process. As already mentioned above, the annealing temperatures (T_A) for the different samples were calculated based on the glass transitions temperatures using Equation 1.

$$T_A = 0,92 * T_g \quad [1]$$

2.5 Hardness

Annealed and cut samples were mounted in epoxy resin. Before microindentation could be done, the samples had to be polished down to a roughness <0.1µm. Although, the roughness wasn't measured, other studies have shown that the last step in Table 4 ensures it is under the mentioned threshold. All grinding and polishing steps were carried out using a MetPrep 4 automatic polisher (Allied High Tech Products Inc., Compton, CA, USA). The polishing schedule, detailing which discs and lubricants used, is shown in Table 4. The solutions used in steps three through ten were poly-diamond glycol suspensions.

Table 4 Finishing Schedule for Grinding/Polishing of Microhardness Samples

Schedule for Microhardness samples					
Disc	Lubricant	Force [N]	RPM Platen	RPM Holder	Time [s]
Step 1					
260µm Diamond	Water	22	150	150	20
Step 2					
70µm Diamond	Water	22	300	150	30
Step 3					

1200 grid SiC paper	Water	22	150	150	2x30
Step 4					
9µm	9µm solution	26/22	150	150	180/120
Step 5					
6µm	6µm solution	22/26	150	150	120/180
Step 6					
3µm	3µm solution	26	150	150	150 (optional 2 nd time)
Step 7					
1µm	1µm solution	22	150	150	150 (optional 2 nd time)
Step 8					
0,5µm	0,5µm solution	22	150	150	150 (optional 2 nd time)
Step 9					
0,25µm	0,25µm solution	22	150	150	120
Step 10					
0,04µm	0,04µm solution	22	150	150	120

The microindentation tests were conducted utilizing a Q60A+ automated microindenter (Qness GmbH, Golling, AT). To ensure the quality of the results, the device was calibrated weekly, using standard test blocks. The tests as well as the evaluation of the results were carried out as described in the standards of the International Organisation of Standardisation (ISO) and the American Society for Testing and Materials (ASTM). [14] [15] [16] In order to fulfil the standards' requirements, the temperature of the room and the equipment used during the tests had to be set to 23°C ± 5°C. In addition, for every load and for every composition at least 5 valid indentations had to be created so that a relevant mean value could be obtained. Furthermore, as suggested in the standards, the holding time at maximum force equalled 10 seconds. The indents were evaluated using Equation 2. In this Equation, P is the force in N and d is the average of the diagonals in mm, resulting in a Vickers micro-hardness (H_V) given in GPa.

$$H_V = 0,0018544 \left(\frac{P}{d^2} \right) \quad [2]$$

For any glass as well as for any ceramic, it is necessary to measure the hardness value at different loads, to observe a hardness-load curve. The reason for this is that these kinds of materials show an indentation size effect (ISE). Materials with an ISE exhibit a higher hardness value at lower loads

which decreases with increasing load, till the hardness reaches a plateau value. [17] [18]The plateau value is often linked to the point where extensive cracking is initiated in the composition. [19] [20] Although known for quite some time, there is still no confirmed explanation on the mechanisms behind the ISE. At this point, the most recognized theory is the Nix-Gao Model. [21] The loads used to measure the hardness during this study were 0.1, 0.2, 0.5, 1, 2 and 5kg.

2.6 Echography and density

In order to evaluate shear modulus and Young's modulus of the compositions an echography test had to be conducted. The test was executed using a 45MG Olympus velocimeter (Olympus Corporation, Tokio, Japan). Before the test could be carried out, both sides of the previously annealed and cut samples had to be ground and polished to at least a roughness $<3\mu\text{m}$. In order to do that, the samples were mounted on metal sockets with the help of mounting wax #71-10040 (Allied High Tech Products Inc., Compton, CA, USA). They also had to be parallel ($\pm 3^\circ$) and clean. As mentioned in Section 2.5, the roughness wasn't measured but other works show that with the last step in Table 5, the threshold will not be exceeded. The polishing schedule used to prepare the samples for echography is shown in Table 5.

Table 5 Grinding/Polishing Schedule for Echography Samples

Schedule for Echography samples					
Disc	Lubricant	Force [N]	RPM Platen	RPM Holder	Time [s]
Step 1					
260 μm Diamond	Water	22	150	150	10
Step 2					
70 μm Diamond	Water	22	300	150	30
Step 3					
1200 grid SiC paper	Water	22	150	150	2x30
Step 4					
9 μm	9 μm solution	26/22	150	150	180/120
Step 5					
6 μm	6 μm solution	22/26	150	150	120/180
Step 6					
3 μm	3 μm solution	26	150	150	150 (optional 2 nd time)

Step 7					
1μm	1μm solution	22	150	150	150 (optional 2 nd time)
Step 8					
0,5μm	0,5μm solution	22	150	150	150 (optional 2 nd time)

Utilizing the velocimeter, the longitudinal material-wave velocity (V_L) and the transverse or shear material-wave velocity (V_T) of the samples in [mm/μs] were measured. To get a more representative value for the longitudinal material-wave velocity (V_L) as well as the transverse/shear material-wave velocity (V_T) three separate measurements were conducted and their mean value calculated. Another reason why the values were determined that way, was that the influence off pores, voids etc. near the surfaces could be minimized. The various moduli of our samples as well as the poisson's ratio were calculated using the following equations:

$$\text{Shear Modulus [Pa]} \quad G = (V_T^2 \rho) \quad [2]$$

$$\text{Poisson's Ratio} \quad \vartheta = \frac{1 - 2 \left(\frac{V_T}{V_L}\right)^2}{2 - 2 \left(\frac{V_T}{V_L}\right)^2} \quad [3]$$

$$\text{Young's Modulus [Pa]} \quad E = 2G(1 + \vartheta) \quad [4]$$

$$\text{Bulk Modulus [Pa]} \quad K = \frac{E}{3(1 - 2\vartheta)} \quad [5]$$

In order to make use of Equation 2 it was necessary to measure the density ρ of the samples in [g/cm³]. This was done by the Archimedes method at room temperature and in water. The density was then calculated using Equation 6:

$$\rho = \frac{m_{dry}}{m_{dry} - m_{wet}} (\rho_{water} - \rho_{air}) + \rho_{air} \quad [6]$$

2.7 Probability of crack Initiation and crack resistance

Probability of crack initiation (PCI) was evaluated for each indent, by counting the number of primary radial cracks (n_{pc}) and divide it by the total number of corners of the indent ($n_{corners}$). This calculation is shown in Equation 7 [22]:

$$PCI = \frac{n_{pc}}{n_{corners}} \quad [7]$$

Examples how primary radial cracks were counted are shown in Figure 2. The two main criteria for how these cracks have been identified were:

- Is the crack emanating from a corner
- Does the crack run parallel to the indent axis

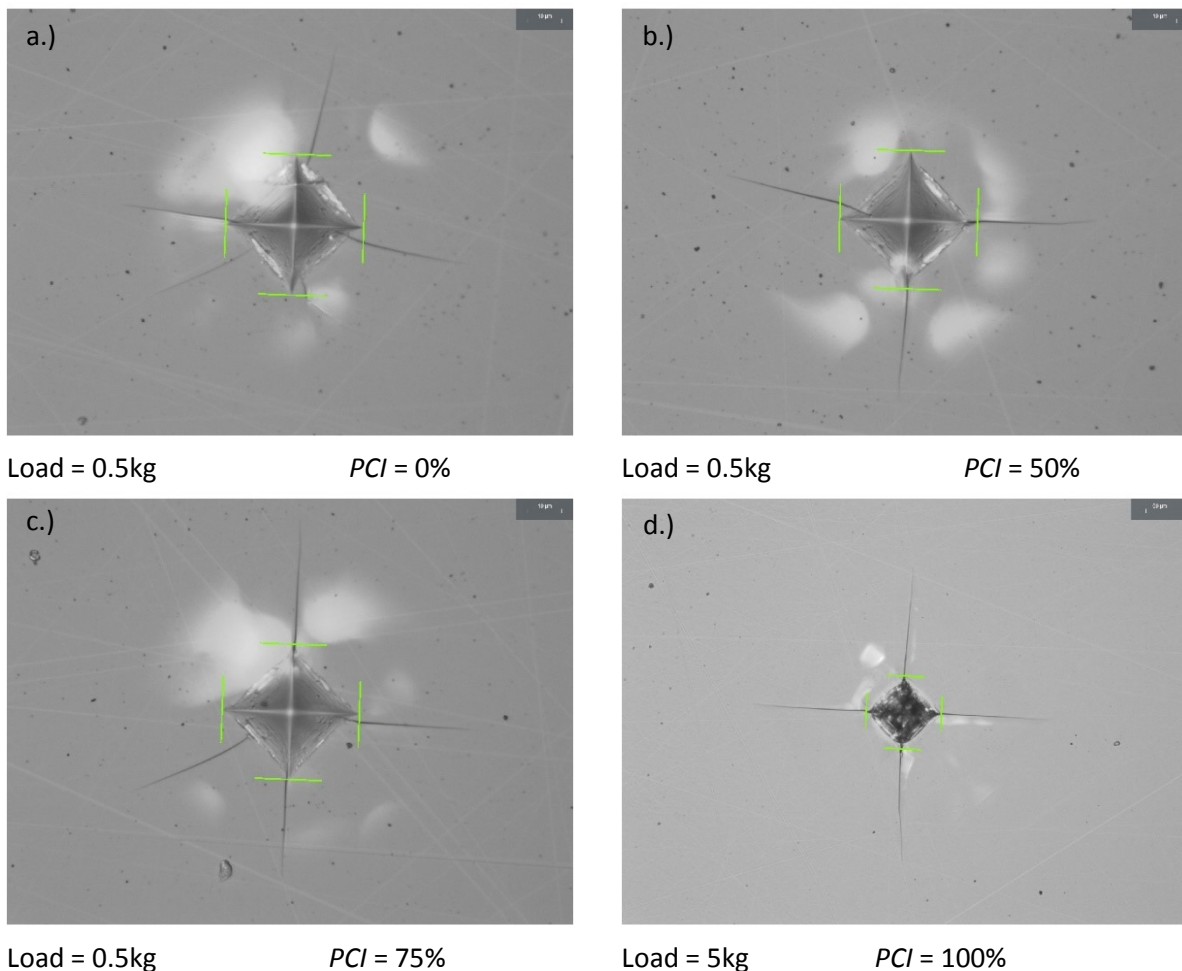


Figure 2 Examples for PCI counting (Ba16)

Neither of the cracks seen in Figure 2 a.); fulfils the criteria above and therefore results in 0% PCI . In Figure 2 b.); three cracks can be observed emerging from the indent, but only two of them start at a corner and then run parallel to the indents axis. This leads to a PCI of 50%. As for Figure 2 c.); four cracks can be observed, but one of those four cracks doesn't fulfil the criteria stated above leading to a PCI of 75% for this indent. All four cracks of the indent shown in Figure 2 d.); start from a corner and run parallel to the axis and therefore this indent has a PCI of 100%.

In the case of Vickers indents, the number of corners is four ($n_{\text{corners}} = 4$). The *PCI* for each load and composition was measured using at least 30 indents in three sets of 10 indents. The pictures of the indents used to count the cracks were taken within 10 minutes after indentation. There were multiple reasons that this procedure was chosen:

- Minimize environmental impacts like subcritical crack growth
- To stay consistent throughout the whole test series
- Capture the indent as close to unloading as realistically possible

Crack resistance (*CR*) was calculated using the *PCI* results. *PCI* measurements were plotted as a function of applied load ($0.1 \leq P \leq 5.0$ kg). Via the following sigmoidal function the values were then fitted [20]:

$$F(P) = 1 - \exp\left[-\left(\frac{P-P_0}{\beta}\right)^m\right] \quad [8]$$

With P_0 being the critical load to initiate primary cracks, β the scaling parameter and m being the Weibull modulus. *CR* was then determined to be the load where *PCI* reached 50%. Mean *CR* and standard deviation were obtained by utilizing the leave-one-out approach of cross validation. [9]

3 Results and discussion

3.1 Compositions

All four compositions were synthesised and as a result, four bubble free glass tiles were produced. The XRD results for the different compositions are shown in Figure 3. The absence of peaks confirms that the produced tiles are indeed in a glassy state.

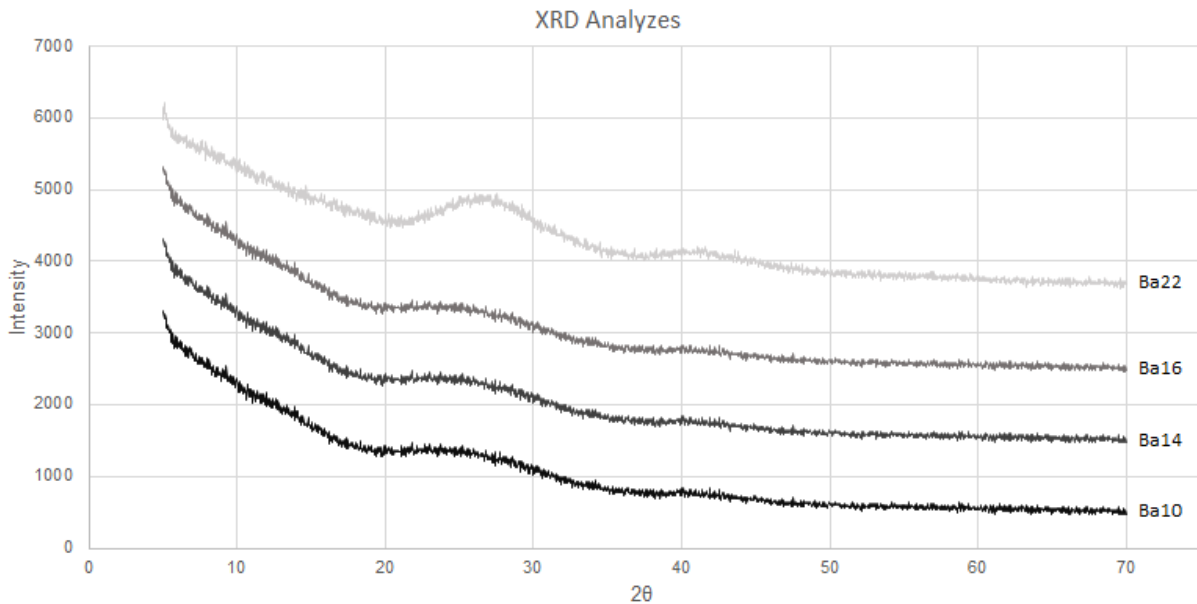


Figure 3 XRD results

The results of the ICP are shown in Table 6.

Table 6 ICP results

#	Composition [mol%]					Molar ratios	
	SiO ₂	B ₂ O ₃	Al ₂ O ₃	BaO	SnO ₂	$\frac{\text{BaO}}{\text{NWFs}}$	$\frac{\text{BaO}}{\text{Al}_2\text{O}_3}$
Ba10	53,13	24,57	10,88	11,29	0,13	0,127	1,03
Ba14	51,16	21,77	10,96	15,82	0,29	0,188	1,44
Ba16	49,61	21,74	11,34	17,16	0,15	0,207	1,51
Ba22	44,44	20,52	11,03	23,86	0,15	0,313	2,16

Comparing the ICP results in Table 6 with the initially designed compositions in Table 2 some observations can be made. Due to dependence on so many factors like the cleanliness of the melt furnace and purity of chemical elements it is not surprising that the batch compositions and the actual compositions differ. In order to fill out the mold corners fast enough and ensure a smooth

pour, high temperatures had to be utilized in order to keep the viscosity of the glasses in an optimal range. With temperatures that high, a certain amount of B_2O_3 is going to volatilize during the melting process, resulting in a net loss of those components in the poured glasses as confirmed in Table 6. Since a portion of B_2O_3 gets lost during melting, the relative portions of SiO_2 , Al_2O_3 and BaO slightly increased in all four compositions.

It is expected; that with increasing $\frac{BaO}{NWFs}$ ratio, more B^{III} will transform into B^{IV} , leading to an overall a rise of tetrahedral boron within the glasses. Since B^{IV} creates a stiffer and more compact structure, the hardness as well as the density should rise with increasing amount of barium in the compositions, meaning the highest density, as well as the highest hardness should be observed for the Ba22 sample.

3.2 Moduli and density

As already mentioned in Section 2.6 the density measurements were conducted utilizing the Archimedes method. In order to get a characteristic value, multiple measurements on different days and on different samples were carried out and a mean density value for each composition was obtained. The details of these measurements, the individual values of each day as well as the mean value for the density of each composition are given in Table 7. It should be mentioned, that the density of the auxiliary liquid was automatically adjusted in the calculations according to the temperature by the measurement device.

Table 7 Density measurement results

Density (ρ)				
	Measurement 1	Measurement 2	Measurement 3	Mean \pm Deviation
	[g/cm ³]	[g/cm ³]	[g/cm ³]	[g/cm ³]
Ba10	2,62	2,64	2,59	2,62 \pm 0,019
Ba14	2,81	2,77	2,80	2,80 \pm 0,015
Ba16	2,82	2,91	2,94	2,89 \pm 0,051
Ba22	3,19	3,21	3,24	3,22 \pm 0,02
Water Temp. [°C]	21,0	21,2	23,1	

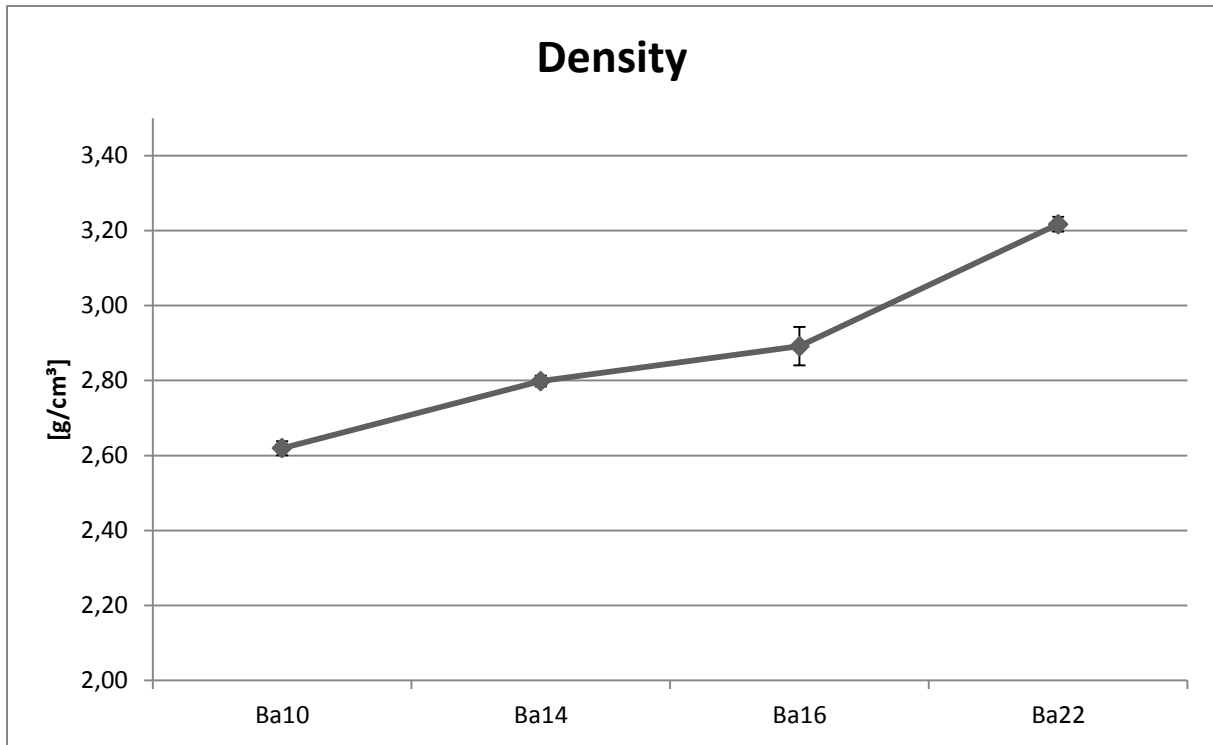


Figure 4 Density with Standard Deviation (note that some error bars are smaller than the markers)

The increase in density with increasing portion of NWM as illustrate in Figure 4 makes sense in a way that barium has the highest molar mass of any element in the designed compositions with 137,327g/mol. Another explanation for the increase in density throughout the series could be given by the statement made in Section 1. Varying the portion of barium included in the composition the more B^{III} converts to B^{IV} which results in a denser, more compact structure overall.

With measured density values of $2.619 \frac{g}{cm^3}$ for Ba10; up to $3.217 \frac{g}{cm^3}$ for Ba22, these compositions show extraordinary high density values compared to other similar aluminoborosilicate glass compositions. Their densities tend to oscillate $\sim 2.3 \frac{g}{cm^3}$. [9] [23] [24]

The results of the measurements for the longitudinal material-wave velocity (V_L) and the transverse/shear material-wave velocity (V_T) as well as their mean value are shown in Table 8.

Table 8 Echography measurement results

Longitudinal Wave Velocity (V_L)				
	Measurement 1	Measurement 2	Measurement 3	Mean \pmDeviation
	[mm/μs]	[mm/μs]	[mm/μs]	[mm/μs]
Ba10	5,25	5,51	5,05	5,27 \pm 0,19
Ba14	5,29	5,25	5,32	5,28 \pm 0,03
Ba16	5,29	5,55	5,62	5,49 \pm 0,14
Ba22	5,56	5,30	5,80	5,55 \pm 0,20
Transverse/Shear Wave Velocity (V_T)				
	Measurement 1	Measurement 2	Measurement 3	Mean \pmDeviation
	[mm/μs]	[mm/μs]	[mm/μs]	[mm/μs]
Ba10	2,78	2,88	2,81	2,82 \pm 0,04
Ba14	2,82	2,84	2,96	2,87 \pm 0,06
Ba16	2,85	2,90	3,12	2,96 \pm 0,12
Ba22	2,73	2,86	2,98	2,85 \pm 0,10

Utilizing the measurement results given in Table 8 in addition to the Equations 2-5 described in Section 2.6 various moduli as well as the Poisson's ratio were calculated for the different compositions. The results of those computations are shown in Table 9.

Table 9 Echography Evaluation results with Error

Moduli Evaluation \pm Error				
	Shear Modulus [GPa]	Poisson's Ratio	Young's Modulus [GPa]	Bulk Modulus [GPa]
Ba10	20,89 \pm 0,23	0,299 \pm 0,006	54,25 \pm 1,22	44,89 \pm 1,34
Ba14	23,24 \pm 0,24	0,290 \pm 0,006	59,95 \pm 1,32	47,54 \pm 1,39
Ba16	24,67 \pm 0,26	0,295 \pm 0,006	63,91 \pm 1,40	52,01 \pm 1,52
Ba22	26,03 \pm 0,27	0,320 \pm 0,006	68,74 \pm 1,52	63,79 \pm 1,87

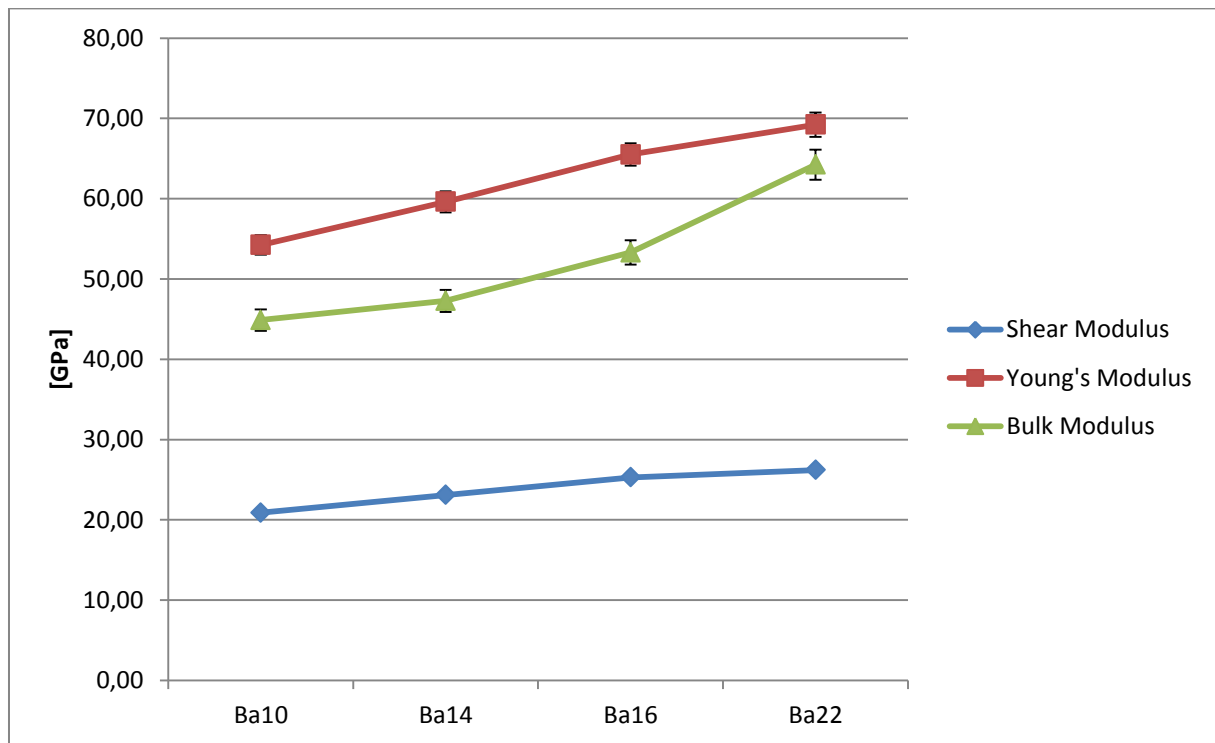


Figure 5 Moduli with Error bars (note that some bars are smaller than the markers)

The results in Table 9 as well as the graphical illustration in Figure 5 show the trends for the various moduli. The most general observation that can be made is that with higher a portion of barium in the composition, shear modulus, Young's modulus as well as bulk modulus are all rising in their value. The shear modulus and Young's modulus values increased around 20% from Ba10 to Ba22. Interestingly, the bulk modulus increased to almost 30% from Ba10 to Ba22. Due to the initial statement made in Section 1 this trend is not surprising at all. The content of NWM in the glass influences the ratio between B^{III} and B^{IV} . Higher fractions for B^{IV} can be reached with higher

amounts of NWM. And since B^{IV} creates a stiffer structure, it makes sense that the composition with the highest amount of NWM has the highest moduli values. Compositions like silica glasses or variations of soda-lime-silica exhibit Young's moduli around 70GPa, shear moduli about 30GPa and bulk moduli up to 44GPa. [3] [25] Compared to these glasses, the compositions investigated during this study show a lower Young's modulus, except for Ba22 which shows similar values for Young's modulus. The same correlation can be observed for the Shear modulus. The bulk modulus however, correlates differently to the compared glasses. In general, high values for the bulk modulus can be observed for the investigated compositions with Ba22 having a bulk modulus of 63.79 ± 1.87 GPa.

The Poisson's ratio values for the different compositions are given in Table 9 and illustrated in Figure 6 show no trend that can be observed within the series. Compared to the Poisson's ratio for silica ($\nu = 0.17$) [3] or soda-lime-silica glasses ($\nu = 0.20 - 0.22$) [25], the compositions investigated in this study show relatively high values for Poisson's ratio ($\nu \approx 0.3$). In Section 3.3 Poisson's ratio and its influence on the researched materials will be discussed further.

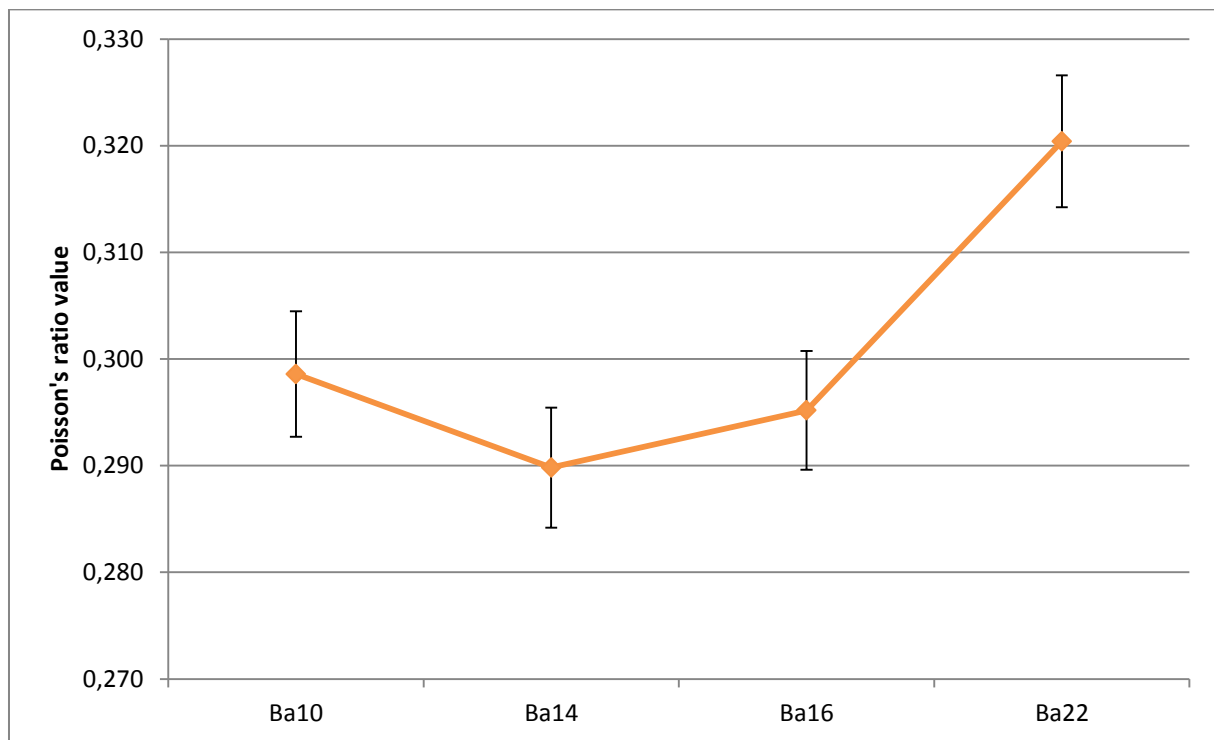


Figure 6 Poisson's ratio with Error bars

3.3 Molar volume and glass transition temperature

For each composition two DSC runs as described in Section 2.4 were conducted. The first experiment was regulated to have a maximum temperature of 1000 °C with a heat rate of 10°C/min. After analysing, the data generated by the first four DSC measurements, it was decided that there was no need for such high temperatures for the second run. The second run for each composition was conducted with a heat rate of 10°C per minute to a maximum temperature of 725°C. T_g was determined after analysing all experiments as a mean value of both measurements for each composition. The results for the glass transition temperatures are shown in Table 10. Molar volume

(V_M) was calculated using the previously measured density and the ICP results. Equation 9 shows the formula used to calculate the molar volume with m_M being the summed molar mass of major components. Results for molar volume are shown in Table 10.

$$V_M = \frac{m_M}{\rho} \quad [9]$$

Table 10 Glass transition temperature with standard deviation and molar volume with error for each composition

Composition	T_g [°C] ±Deviation	V_m [$\frac{\text{cm}^3}{\text{mol}}$] ±Error
Ba10	598,49 ±3,14	29,64 ±0,41
Ba14	624,01 ±1,85	29,22 ±0,39
Ba16	638,38 ±0,79	28,72 ±0,37
Ba22	637,31 ±3,06	27,68 ±0,34

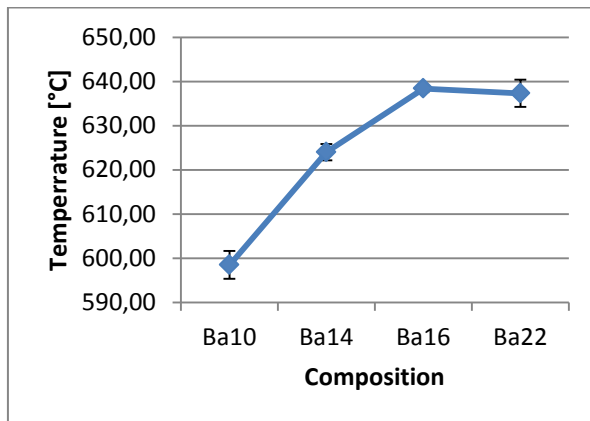


Figure 7 T_g for all four compositions with standard deviation

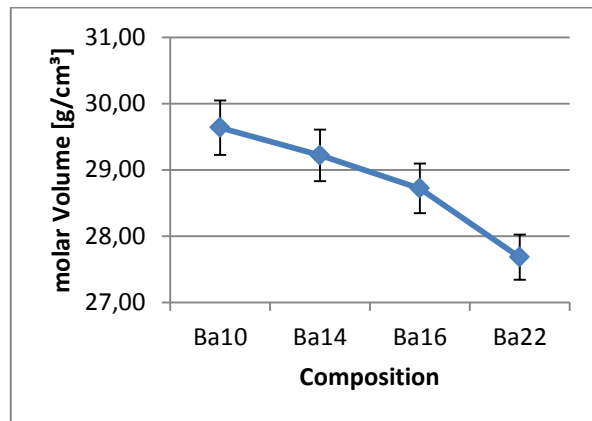


Figure 8 Molar volume with error bars four all four compositions

Figure 7 showcases the trend for T_g for the four compositions. Going up at first, the glass transition temperature reaches a plateau value at Ba16 and Ba22. While this behaviour might seem odd at first, Avramov et al. [26] found an explanation for this trend in glasses containing boric acid. Boric acid consists of BO^3 triangles. By adding NWM the coordination number of boron changes, forming BO^4 tetrahedra, with lower mobility than BO^3 , explaining the rise in T_g . By adding more NWM the oxygen bridges of the BO^4 tetrahedra are broken up. Since these particles can move faster than BO^3 triangles, the glass transition temperature is going to fall at high amounts of NWM. However, so far this behaviour has only been found to start at fractions of NWM of 30%. [26] An explanation why this behaviour already takes place at 20% NWM might be that the other elements within the composition influence T_g more than anticipated and therefore are responsible for the shift.

Figure 8 shows the trend for the molar volume within the series. A monotonic decrease with increasing NWM can be observed between the four compositions. Compositions with higher fractions of BaO exhibit lower values for molar volume. This is not surprising since barium is by far the heaviest element used for synthesis these materials. However, when comparing the molar volume to the Poisson's ratio, a new trend can be observed, as showcased in Figure 9.

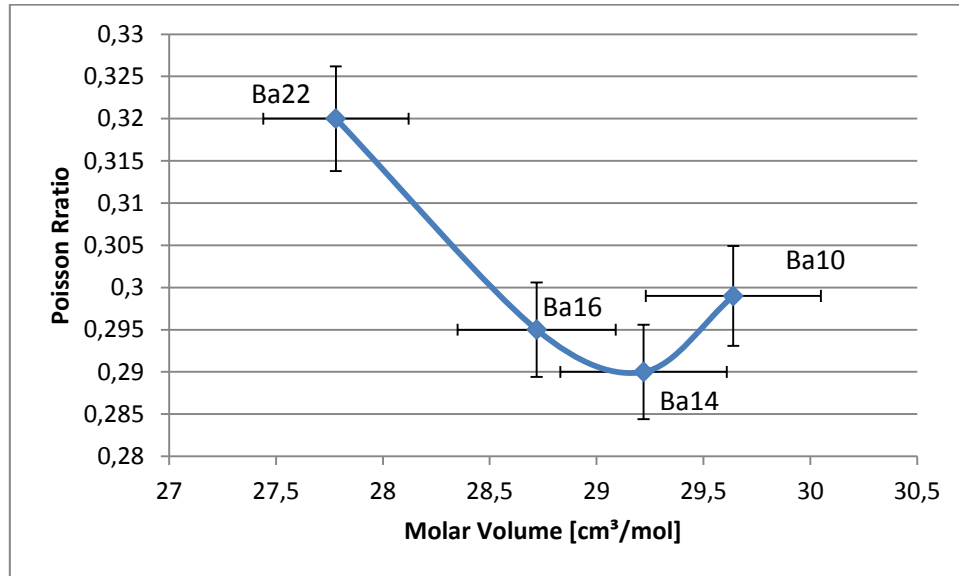


Figure 9 Poisson's ratio over molar volume with error bars

Although the absolute values might not be distinguishable from each other, a very interesting tendency within the series can be seen which doesn't come to mind intuitively. Januchta et al. [27] argued that materials with a closely packed structure (materials with low molar volume) should show small volume changes when changing shape, since there is no room for densification. This behaviour should then present itself in high values for Poisson's ratio. As seen in Figure 9, this correlation is true for three of the four compositions (e.g. Ba14, Ba16 and Ba22). However, Ba10 exhibits a higher ν value than Ba14 and Ba16 despite having the highest molar volume of all four samples. An explanation for this could be given by Rouxel [28], who argued that the connectivity of a material also plays a critical role for the dimension of the Poisson's ratio. Further investigations need to be conducted to give a precise explanation for the trend observed in Figure 9.

3.4 Microhardness and indentation fracture resistance K_{IFR}

3.4.1 Microhardness results

All indentations were made according to ASTM C1327 [15]. The temperature during the tests was held between 20.5 and 21.5°C and the relative humidity had values between 30 and 40%. As mentioned in Section 2.5, glasses tend to have an indentation size effect. Because of this, the hardness values of the samples were measured for various loads. For each composition as well as for every load 30 indents were made, which led to an initial total of 720 indents. After conducting the hardness tests, they were validated according to ASTM C1327 [15]. Out of 30 indents all combinations of composition and loads produced at least 15 valid values, except for two. Samples containing ~24mol% BaO according to ICP, which were loaded with either 1kg or 2kg were nearly impossible to validate due to a mixture of incoming light and reflection off the material. For each of those two combinations, 30 additional indents were produced with different light settings. After

changing the settings, at least 15 indents could also be validated. The hardness values as well as the standard deviations for each combination of compositions and load are shown in Table 11. Figure 10 illustrates the hardness-load curves for each material and shows the ISE.

Table 11 Vickers hardness results with their standard deviation

Composition	Load [kg]					
	0,1	0,2	0,5	1	2	5
Ba10 [GPa]	5,07	4,81	4,66	4,41	4,31	4,46
Deviation	±0,11	±0,06	±0,06	±0,04	±0,07	±0,08
# valid	22	20	17	20	20	16
<hr/>						
Ba14 [GPa]	5,75	5,55	5,28	5,05	4,94	4,96
Deviation	±0,09	±0,06	±0,05	±0,05	±0,05	±0,06
# valid	26	26	17	18	21	18
<hr/>						
Ba16 [GPa]	6,03	5,87	5,66	5,42	5,35	5,32
Deviation	±0,14	±0,11	±0,13	±0,07	±0,12	±0,09
# valid	19	17	15	17	17	17
<hr/>						
Ba22 [GPa]	6,31	6,13	6,02	5,75	5,72	5,44
Deviation	±0,12	±0,08	±0,08	±0,11	±0,11	±0,1
# valid	22	20	16	16	20	15

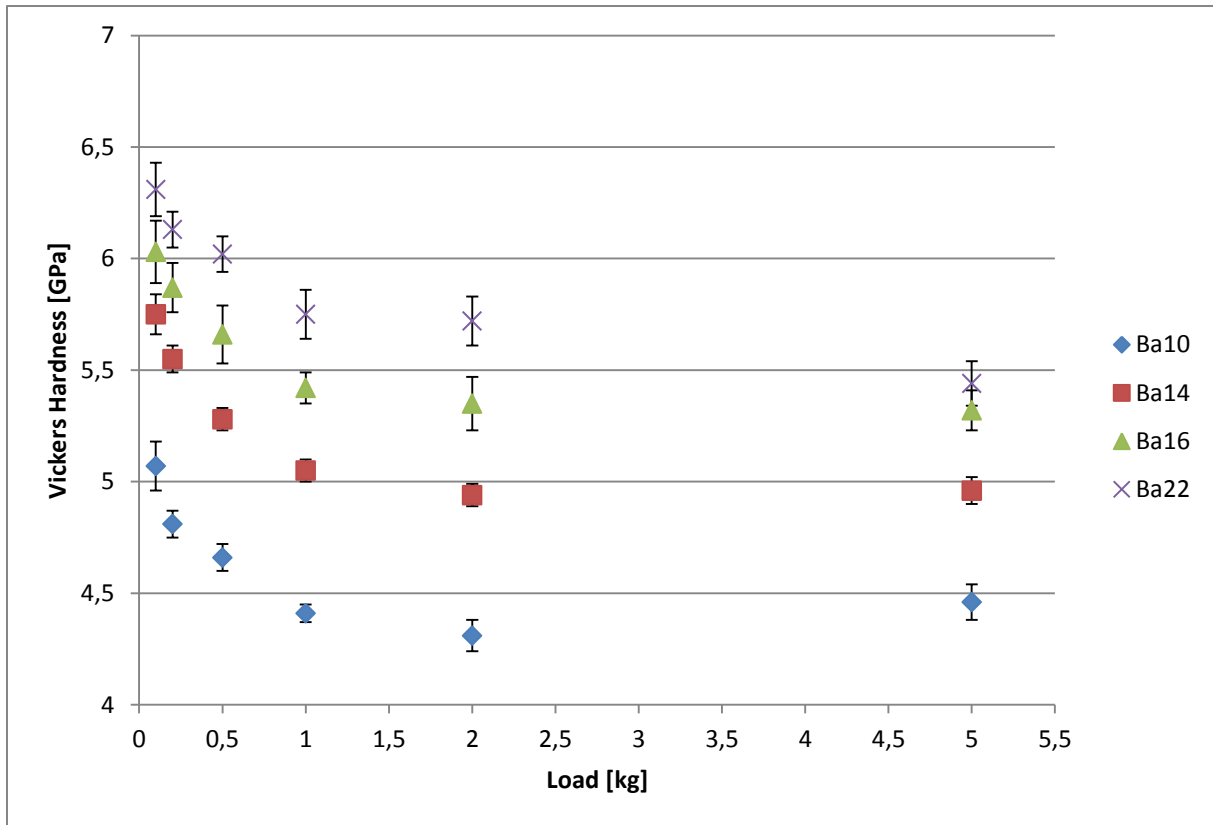


Figure 10 Vickers hardness-load curves (note that some error bars are smaller than the markers)

To compare the present compositions a bit better with each other, as well as with other comparable glass products, the Vickers hardness values at 0.5kg for the four materials are plotted in Figure 11. In addition, the hardness values for a commercial soda-lime-silica glass ($HV_{0.5} \approx 5.4 \pm 0.1 \text{ GPa}$), a commercial borosilicate ($HV_{0.5} \approx 5.31 \pm 0.04 \text{ GPa}$) and a composition called Ba12 ($HV_{0.5} \approx 4.74 \pm 0.03 \text{ GPa}$) produced by Fry et al., [9] which consists of the same raw materials as the current compositions containing ~12mol% BaO are also shown in Figure 11.

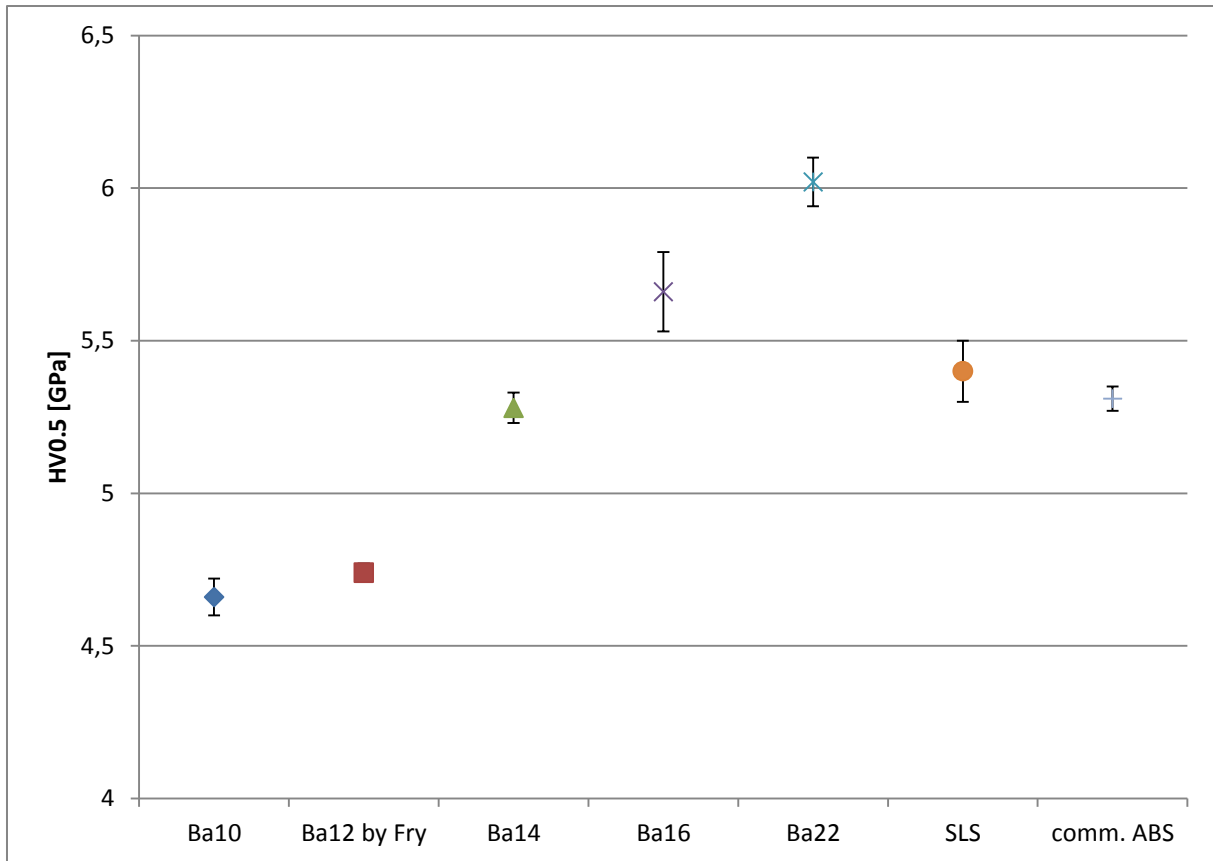


Figure 11 Vickers hardness [Load = 0.5kg] for different materials with their standard deviation

Both Figure 10 and Figure 11 show that Ba22 ($HV_{0.5} = 6.02 \pm 0.08 \text{ GPa}$) has the overall highest hardness while Ba10 ($HV_{0.5} = 4.66 \pm 0.06 \text{ GPa}$) has the lowest. These results suit well with the hypothesis made earlier that B^{IV} plays a critical role for the hardness of ABS glasses. It suggests that these kinds of products get harder the higher the fraction of B^{IV} within the composition is. Another observation that can be made is that the Ba12 ($HV_{0.5} \approx 4.74 \pm 0.03 \text{ GPa}$) produced by Fry et al. [9] fits the trend that is seen with the four initial compositions. Figure 11 also shows, with the correct amount of BaO, hardness values can be reached which surpass nowadays commercially used glass compositions. Depending on the field of application this information can be very useful moving forward.

3.4.2 Indentation fracture resistance (K_{IFR})

The idea to determine a toughness value for a material via the length of the cracks induced by Vickers indents was first recognized by Palmqvist in 1957 and has since been the topic of various studies. [29] [30] Especially for materials where the Vickers indentation test is used frequently to evaluate the hardness of the compositions, it seems very convenient to use the resulting cracks to get more information while only having to conduct one test. Despite many advantages, e.g. time and cost efficiency, there are a lot of negative aspects to the method. The main disadvantage is namely the offset between the indentation fracture resistance measured with this method and the fracture toughness as measured with tests like SEVNB, SCF or CNB. [31] [32] [33] So, while the indentation fracture resistance test might not be able to give an accurate fracture toughness value for the materials used in this study it should show the trend between compositions.

The Vickers indents were conducted as described in Section 3.4.1. The validation of cracks, their measurements, as well as their evaluation were carried out as specified in ISO 14627:2012. [34] It was only possible to use indents made with $P=5.0\text{kgf}$, since those were the only ones that showed consistent evenly cracking on all four corners of the Vickers imprint. While the Ba14, Ba16 and Ba22 samples showed at least eight valid values (8, 13 and 11, respectively), the Ba10 compositions only had three valid imprints according to ISO 14627 to work with. The results for the indentation fracture resistance are shown in Table 12 and the trend is illustrated in Figure 12.

Table 12 Indentation fracture resistance values and their standard deviation

	Ba10	Ba14	Ba16	Ba22
$K_{IFR} \left[\text{MPam}^{\frac{1}{2}} \right]$	1,08	1,03	0,99	0,83
Standard deviation $\left[\text{MPam}^{\frac{1}{2}} \right]$	$\pm 0,05$	$\pm 0,03$	$\pm 0,03$	$\pm 0,04$

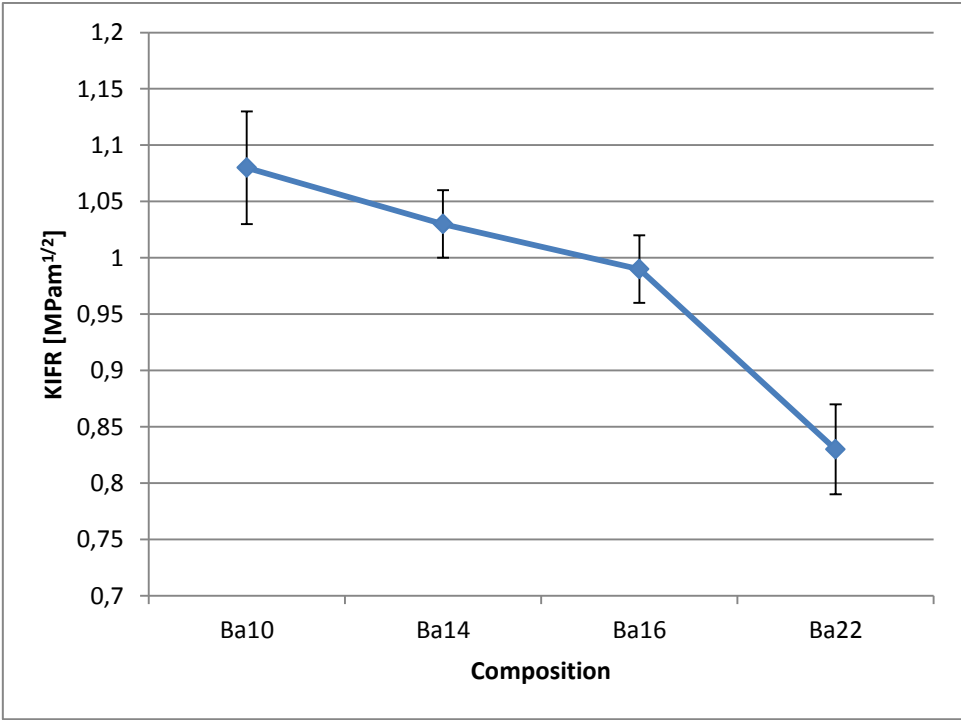


Figure 12 Indentation fracture resistance trend between compositions

Both Table 12 and Figure 12 show that Ba10 ($K_{IFR} = 1,08 \pm 0,05 \text{MPa}^{\frac{1}{2}}$) has the highest and Ba22 ($K_{IFR} = 0,83 \pm 0,04 \text{MPa}^{\frac{1}{2}}$) has the lowest indentation fracture resistance. The trend observed in Figure 12 agrees well with the statements made in Section 1. B^{IV} forms a denser and stiffer structure

than B^{III} and is thus more prone to cracking. The compositions investigated in this study show relatively high values of K_{IFR} compared to other glasses, including soda-lime-silica and aluminoborosilicate glasses ($K_{IFR} = 0,70 - 1,05 \pm 0,04 \text{MPa}^{\frac{1}{2}}$). [35] While this gives a tendency, to get more meaningful and comparable values for fracture toughness, other, more recognized, fracture toughness tests like the SEVNB need to be conducted in the future.

3.5 Crack resistance

Figure 13 shows how the *PCI* data was modelled and analysed in the case of Ba16. The raw data points, as well as the standard deviation were generated by using the mean *PCI* value of three sets of 10 indents. This was done for all six loads ($P=0.1-5.0\text{kgf}$). Based on the raw data and utilizing Equation 8 a sigmoidal fit was generated. Both the raw data as well as the fit are illustrated in Figure 13. The line at 50% *PCI* marks the crack resistance (*CR*) for the composition.

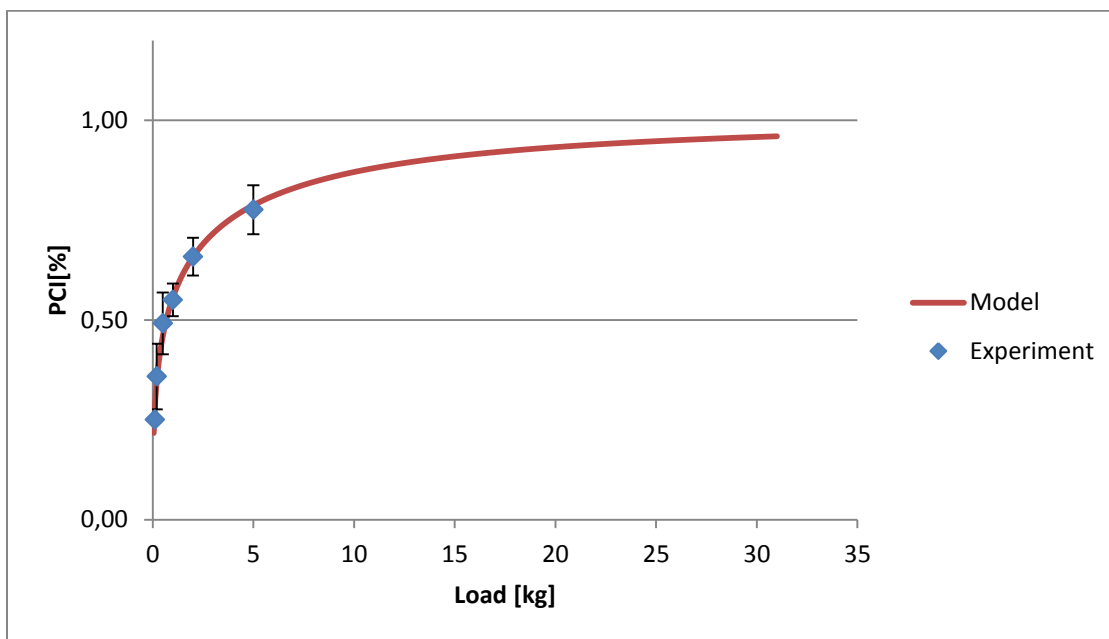


Figure 13 *PCI* results with error bar and the fitted model for Ba16

To get a more accurate *CR* value as well as a standard deviation, six more fits for each composition were generated using the “leaving-one-out” method of cross validation. The *CR* results for all four glasses as well as the fitting parameters are shown in Table 13 and illustrated in Figure 14.

Table 13 *CR* results and fitting parameter for all compositions

Glass	<i>CR</i> [kg]	Deviation [kg]	<i>m</i> [-]	β [-]
Ba10	5,01	0,76	1,28	66,25
Ba14	3,44	0,64	1,47	45,90
Ba16	0,70	0,04	0,40	16,63
Ba22	???	???	48,12	0,98

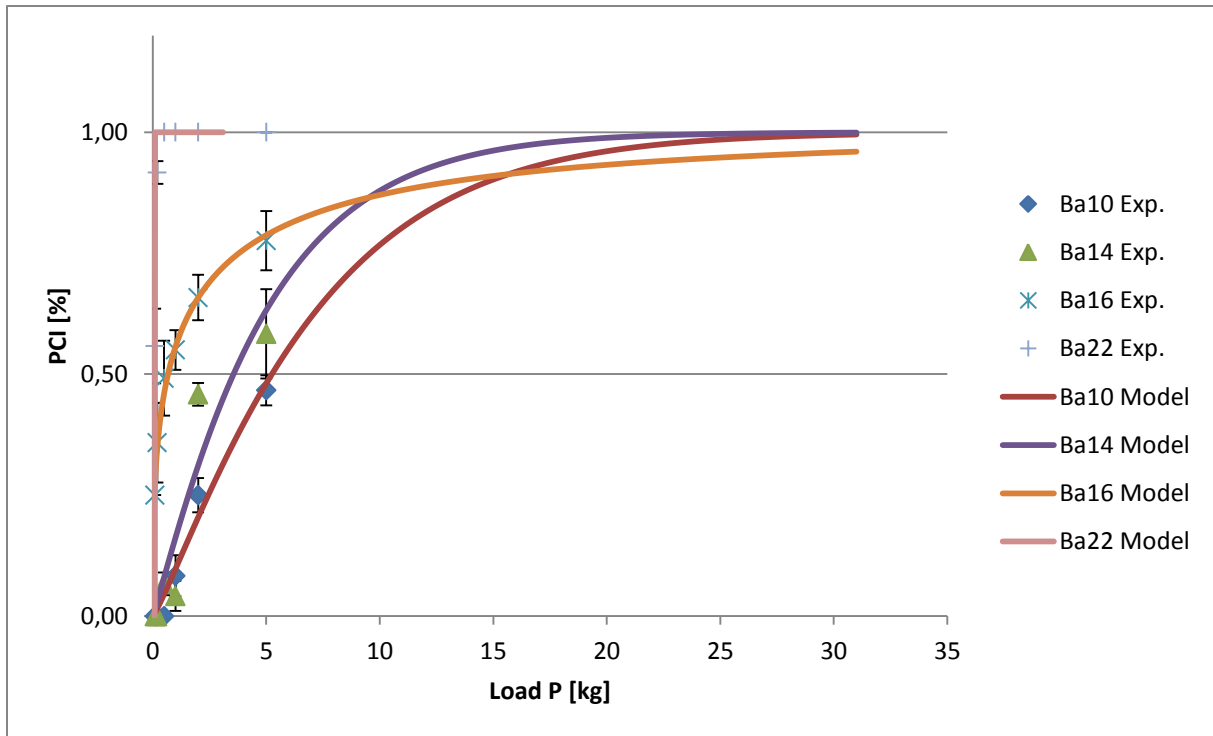


Figure 14 Experimental and modelled *PCI* for all compositions

Table 13 and Figure 14 showcase that *CR* seems to be correlated inversely with the portion of BaO in the glass, meaning that increasing BaO leads to lower values for *CR*. In Section 3.4.1, hardness results as well as the trends for the glasses have already been discussed. It seems convenient that glasses with high hardness or high fractions of BaO have a low value for *CR* since it is well known that materials with high hardness tend to exhibit high brittleness. [27] These findings also suit the fact observed in Section 3.4.2 that high values for indentation fracture resistance are observed in compositions with low barium oxide content. All these findings show that the ratio between B^{III} and B^{IV} plays a critical role for crack resistance.

In the special case of Ba22, no value for *CR* could be evaluated. The model used wasn't able to process the data properly and no meaningful value for crack resistance could be obtained. The model evaluated *PCI* to either be 0% for no applied load or 100% for applied loads >0kg, meaning as far as the model is concerned, the glass will produce at least two primary cracks 100% of the time when exposed to any load, no matter how small. The fitting parameters of Ba22 change wildly compared to the other three compositions. This could be because Ba22 might be so brittle that it doesn't behave like the other 3 compositions and can therefore not be described with the model used.

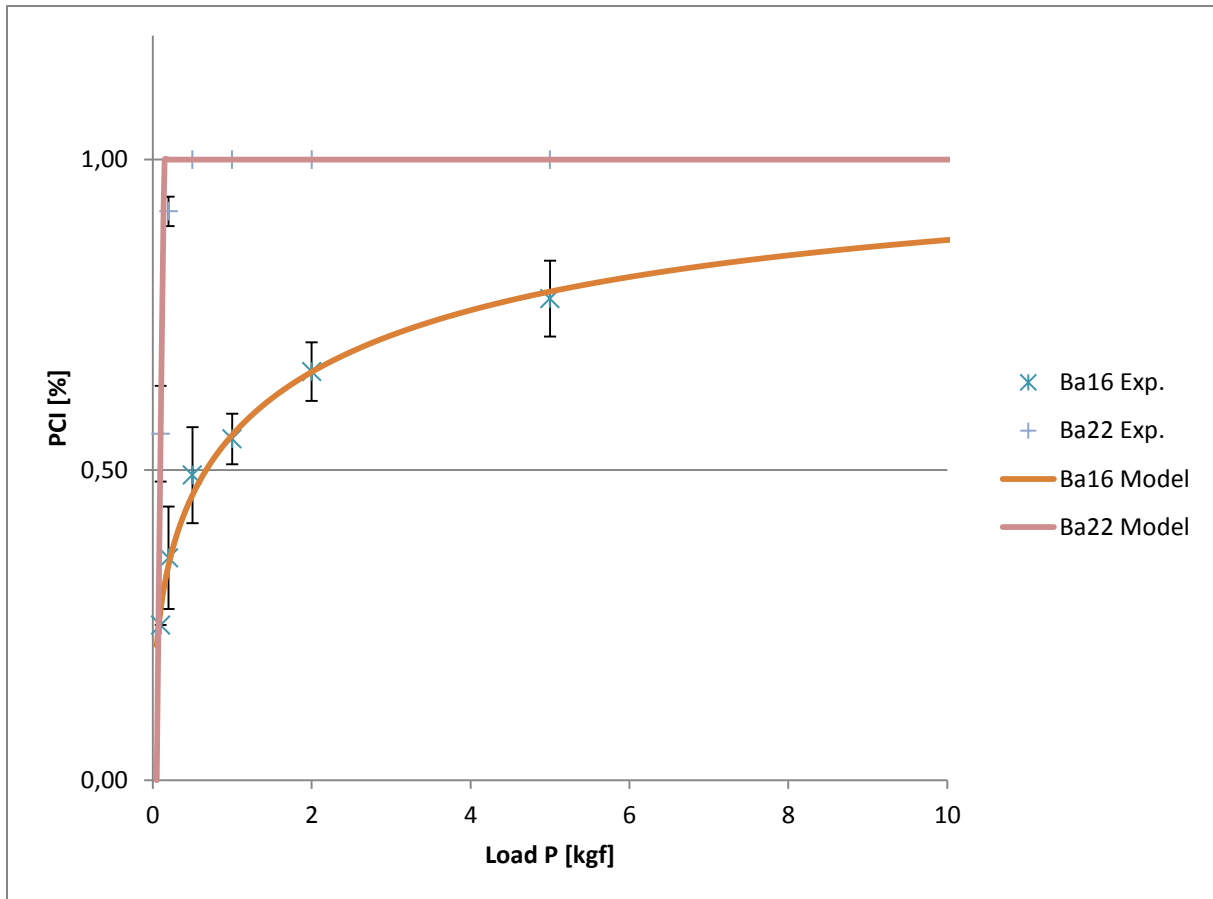


Figure 15 Zoomed in view of experimental and modelled *PCI* for Ba16 and Ba22

Taking a closer look at Figure 15 and comparing the experimental data from Ba16 with Ba22, an interesting fact can be observed. The *PCI* value for Ba16 at the smallest load is 24%, which continuously rises with higher loads, crossing the previously defined threshold for *CR* and eventually reaching 100% at high enough loads. The experimental data for Ba22 however shows, that at the smallest load ($P = 0.1\text{kgf}$), a *PCI* of 56% can be seen. Meaning that already at this load the threshold for *CR* as defined earlier has been crossed. This complements the other experiments conducted as a part of this study, which indicate the high brittleness of Ba22. To get a *CR* value for Ba22 and help the model get a better fit, further experiments have to be conducted with loads $< 0.1\text{kgf}$, ideally ranging from 0.01kgf to 0.09kgf with steps of 0.02kgf .

4 Conclusion

Four different ABS glass compositions were designed and the influence that the portion of NWM has on the physical and mechanical properties of the resulting glass was examined. Each composition resulted in bubble free glass samples with compositions close to the initially intended design as confirmed via inductively coupled plasma atomic emission spectroscopy. The glassy state of the samples was verified via X-ray diffraction analysis. Various experiments were conducted to determine the physical and mechanical properties of each composition.

While Vickers hardness, density as well as the Young's, shear, and bulk moduli tend to increase with higher portions of NWM, other properties like crack resistance and indentation fracture resistance decrease. These trends were generally expected and solidify the statement given in Section 1 that the addition of NWM leads to a change in structure, namely the transformation of boron units from B^{III} to B^{IV} resulting in more compact, rigid glassy network.

As for the Poisson's ratio, no trend within in the series can be observed on its own. Although the absolute values might not be distinguishable from each other, in combination with the molar volume; however, an interesting tendency can be examined. At first an expected trend can be observed in which case low molar volume leads to high values for Poisson's ratio. Between Ba14 and Ba10 a shift in the trend takes place where the Poisson's ratio increases as the molar volume increases as well. This doesn't make sense intuitively since high molar volume should mean more room for densification and thereby lead to low values for Poisson's ratio.

For the glass transition temperature a plateau value has been observed which initially wasn't expected. However some studies suggest that this behaviour might occur due to the formation of non-bridging oxygens at high portions of NWM in boric acid glasses in which case the glass transition temperature is supposed to decrease. However, the threshold for this tendency has found to be fractions of NWM of 30%. Do, this doesn't quite explain why this plateau value is already reached at NWM contents of 20%. It might be a possibility that the other elements in the compositions (e.g. alumina) led to a shift of the trend and the decrease of the glass transition temperature already starts at lower portions of NWM.

Future works should look more into the relationship between molar volume and Poisson's ratio as well as get a more detailed idea about how the different elements in ABS glasses influence the glass transition temperature.

5 Reference

- [1] A. MacFarlane und G. Martin, *Glass A World History*, Chicago: University of Chicago Press; First Edition, 2002.
- [2] „INTERNATIONAL YEAR OF GLASS,“ [Online]. Available: <https://www.iyog2022.org/>. [Zugriff am 4 May 2023].
- [3] A. Vashneya und J. Mauro, *Fundamental of Inorganic Glasses (Third Edition)*, Amsterdam: Elsevier, 2019.
- [4] A. K. Varshneya und J. C. Mauro, „Comment on Misconceived ASTM Definition of "Glass" by A.C. Wright,“ *Glass Technology - European Journal of Glass Science and Technology Part A*, pp. 28-30, 1 February 2010.
- [5] M. C. Onbaşlı, A. Tandia und J. C. Mauro, „Mechanical and Compositional Design of High-Strength Corning Gorilla® Glass,“ in *Handbook of Materials Modeling*, Berlin, Springer, Cham, 2020, p. 23.
- [6] J. C. Mauro, A. Tandia, K. Deenamma Verghese, Y. Z. Mauro und M. M. Smedskjaer, „Accelerating the Design of Functional Glasses through Modeling,“ *American Chemical Society*, pp. 4267-4277, 3 June 2016.
- [7] E. Zanotto und F. Coutinho, „How many non-crystalline solids can be made from all the elements of the periodic table?,“ *Journal of Non-Crystalline Solids*, pp. 285-288, 2004.
- [8] M. Ediger und P. Harrowell, „Perspective: Supercooled liquids and glasses,“ *The Journal of Chemical Physics*, pp. 137-151, Augst 2012.
- [9] A. Fry, C. George, I. Slagle, H. Hawbaker, S. Feller und S. Kim, „Field strength effect on structure, hardness, and crack resistance in single modifier aluminoborosilicate glasses,“ *J Am Ceram Soc.*, pp. 1-16, 2022.
- [10] M. Lima und R. Monteiro, „Characterisation and thermal behaviour of a borosilicate glass,“ *Thermochimica Acta*, pp. 69-74, 2001.
- [11] G. Jellison, L. W. Panek, P. J. Bray und G. B. Rouse, „Determinations of Structure and Bonding in Vitreous B₂O₃ by means of B₁₀, B₁₁ and O₁₇ NMR,“ *J. Chem. Phys.*, pp. 802-812, 1977.
- [12] R. E. Youngman, S. T. Haubrich, J. W. Zwanziger, M. T. Janicke und B. F. Chmelka, „Short- and Intermediate-Range Structural Ordering in Glassy Boron Oxide,“ *Science*, pp. 1416-1420, 1995.
- [13] „cs.mcgill,“ [Online]. Available: <https://www.cs.mcgill.ca/~rwest/wikispeedia/wpcd/wp/b/Barium.htm#:~:text=Barium%20carbonate%20is%20used%20in,used%20extensively%20in%20rubber%20production..> [Zugriff am 16 May 2023].

- [14] ASTM E384:1997, „Standard test Method for Microhardness of Materials“.
- [15] ASTM C1327:2019, „Standard Test Method for Vickers Indentation Hardness of Advanced Ceramic“.
- [16] ISO 14705:2016, „Fine ceramics (advanced ceramics, advanced technical ceramics) - Testmethod for hardness of monolithic cceramics at room temperature“.
- [17] P. Sellappan, T. Rouxel, F. Celarie, E. Becker, P. Houizot und . R. Conradt, „Composition dependence of indentation deformation and indentation cracking in glass,“ *Acta Materialia* 61, pp. 5949-5965, 2013.
- [18] Y. Milman, A. Golubenko und S. Dub, „Indentation size effect in nanohardness,“ *Acta Materialia*, pp. 7480-7487, December 2011.
- [19] T. Rouxel, P. Sellappan, F. Célarié, P. Houizot und J.-C. Sanglebœuf, „Toward glasses with better indentation cracking resistance,“ *Comptes Rendus Mécanique*, pp. 46-51, 2014.
- [20] A. Pönitzsch, M. Nofz, L. Wondraczek und J. Deubener, „Bulk elastic properties, hardness and fatigue of calcium aluminosilicate glasses in the intermediate-silica range,“ *Journal of Non-Crystalline Solids*, pp. 1-12, 2016.
- [21] G. M. Pharr, E. G. Herbert und Y. Gao, „The Indentation Size Effect: A Critical Examination of Experimental Observations and Mechanistic Interpretations,“ *Annual Review of Materials Research*, pp. 271-92, 2010.
- [22] G. A. Rosales-Sosa, A. Masuno, Y. Higo und H. Inoue, „Crack-resistant Al₂O₃-SiO₂glasses,“ *Scientific Reports*, pp. 1-7, 07 April 2016.
- [23] M. Prado, N. Messi, T. Plivelic, I. Torriani, A. Bevilacqua und M. Arribere, „The effects of radiation on the density of an aluminoborosilicate glass,“ *Journal of Non-Crystalline Solids*, pp. 175-184, 2001.
- [24] L. Zhang, J. Kang, J. Wang, G. Khater, Q. Shi, S. Li, J. Zhao, J. Teng und Y. Yue, „Effects of Y₂O₃ on structure and dielectric properties of aluminoborosilicate glasses,“ *Journal of Non-Crystalline Solids*, pp. 110-114, 2019.
- [25] E. Kilinc und R. Hand, „Mechanical properties of soda-lime-silica glasses with varying alkline earth contents,“ *Journal of Non-Crystalline Solids*, pp. 190-197, 2015.
- [26] I. Avramov, T. Vassilev und I. Penkov, „The glass transition temperature of silicate and borate glasses,“ *Journal of Non-Crystalline Solids*, pp. 472-476, March 2005.
- [27] K. Januchta, M. Bauchy, R. E. Youngman, S. J. Rzoska, M. Bockowski und M. M. Smedskjaer, „Modifier field strength effects on densification behavior and mechanical properties of alkali aluminoborate glasses,“ *Physical Reviw Materials*, 2017.

- [28] T. Rouxel, „Elastic Properties and Short-to Medium-Range Order in Glasses,“ *Journal of the American Ceramic Society*, pp. 3019-3039, 18 September 2007.
- [29] T. Lube, „Indentation crack profiles in silicon nitride,“ *Journal of European Ceramic Society*, pp. 211-218, 2001.
- [30] S. Palmqvist, „Indentation hardness and fracture toughness in single crystal,“ *Jernkontorets Annaler*, pp. 300-307, 1957.
- [31] C. Ponton und R. Rawlings, „Vickers indentation fracture toughness test Part 1 Review of literature and formulation of standardised indentation toughness equations,“ *Materials Science and Technology*, pp. 865-873, September 1989.
- [32] ISO 23146:2012, „Fine ceramics (advanced ceramics, advanced technical ceramics) - Test methods for fracture toughness of monolithic ceramics - Singl-edge V-notch beam (SEVNB) method“.
- [33] ASTM C1421:2018, „Standard Test Method for Determination of Fracture Toughness of Advanced Ceramics at Ambient Temperature“.
- [34] ISO 14627:2012, „Fine ceramics (advanced ceramics, advanced technical ceramics) — Test method for fracture resistance of silicon nitride materials for rolling bearing balls at room temperature by indentation fracture (IF) method“.
- [35] S. Dériano, A. Jarry, T. Rouxel, J.-C. Sangleboeuf und S. Hampshire, „The indentation fracture toughness (K_{IC}) and its parameters: the case of silica-rich glasses,“ *Journal of non-crystalline solids*, pp. 44-50, 2004.